PAPER

Check for updates

Spontaneous generation of an atomically dispersed Mo and MoS₂ coupling catalyst *via* reaction induction transformation for enhancing local hydrogen concentration in hydrogenation†

Guangxun Sun,[a] Peng Xue,[a] Changle Yue,[a] Yang Li,[a] Hongfu Shi,[a] Xin Zhang,[a] Fengyu Tian,[a] Junxi Li,[a] Zekun Guan,[a] Bin Liu,[a] Zhi Liu,*[c] Yunqi Liu*[ab] and Yuan Pan ✪ *[a]

The development of a synergistic coupling catalyst at the atomic scale for slurry-phase hydrogenation of vacuum residue (VR) is extremely challenging. Herein, we designed and constructed a robust coupling catalyst comprising Mo single atoms and MoS₂ (Mo SAs–MoS₂) using a reaction induction transformation strategy. The spontaneous generation of Mo SAs–MoS₂ synergistically promoted H₂ activation and enhanced local active hydrogen concentration in the hydrogenation of VR. Benefiting from the strong hydrogen concentration distribution in MoS₂ and Mo SAs, the catalyst revealed remarkable hydrogenation performance toward VR with a TOF$_T$ of up to 0.39 s^{-1}, liquid product yield of 92 wt%, and coke content of 0.6 wt%. Theoretical calculations revealed that the synergistic action of Mo SAs–MoS₂ facilitated electron transfer between Mo species and reactants, reducing the desorption energy barriers for H₂ and anthracene and thereby promoting the hydrogenation of VR. This work provides a novel idea for the design of efficient coupling catalysts for strengthening local active hydrogen concentration in the hydrogenation of VR, and this concept can be applied to other hydrogenation systems.

Broader context

In this study, we designed and constructed a robust coupling catalyst comprising Mo single atoms (SAs) and MoS₂ (Mo SAs–MoS₂) using a reaction induction transformation strategy. The spontaneous generation of the Mo SAs–MoS₂ coupling catalyst synergistically promotes H₂ activation and enhances local active hydrogen concentration in the hydrogenation of vacuum residue (VR). The Mo SAs–MoS₂ catalyst demonstrates superior catalytic hydrogenation activity for the hydrocracking of VR. Benefiting from the strong hydrogen concentration distribution in MoS₂ and Mo SAs, the catalyst demonstrates superior catalytic hydrogenation activity, with a TOF$_T$ of up to 0.39 s^{-1} calculated for total metals, a liquid product yield of 92 wt%, and coke content of only 0.6 wt%. This work proposes a novel concept for the design and development of high-performance hydrogenation catalysts.

Introduction

With the increasing demand for light fuel oils,[1] efficiently converting and cleanly utilizing vacuum residue (VR) has become a crucial focus in the refining industry.[2] Slurry-phase

[a] *State Key Laboratory of Heavy Oil Processing, China University of Petroleum (East China), Qingdao 266580, China. E-mail: panyuan@upc.edu.cn*

[b] *School of Chemistry and Materials Science, Anhui Normal University, Wuhu 241002, China*

[c] *State Key Joint Laboratory of Environment Simulation and Pollution Control, Research Center for Eco-Environmental Sciences, Chinese Academy of Sciences, Beijing 100085, China*

† Electronic supplementary information (ESI) available. See DOI: https://doi.org/10.1039/d5ey00086f

hydrogenation technology is promising for converting heavy oil into lightweight oil.[3] Efficient hydrogenation can better avoid coking of oil and improve the yield of the liquid product.[4,5] Therefore, the development of high-performance hydrogenation catalysts is the key to realizing the activation of hydrogen molecules and the hydrogenation of macromolecular free radicals in hydrocracking.

At present, the main types of catalyst used are molybdenum sulfide catalysts.[6–8] In hydrogenation, a catalyst precursor is converted into a MoS₂ active phase through *in situ* sulfidation.[9,10] However, the MoS₂ active phase gradually grows and aggregates during the hydrogenation reaction, leading to gradual deactivation of the catalyst.[11] Regarding this issue, our team previously proposed Mo-based single-atom catalysts

(SACs) for enhancing the slurry-phase hydrogenation performance of VR.[12,13] Compared with nanocatalysts, SACs have more exposed active sites and specific coordination structures that can efficiently activate hydrogen molecules, resulting in their better activity and selectivity in hydrogenation reactions.[14–19] However, in complex catalytic reactions, it is often difficult to adsorb macromolecular reactants at a single active site.[20,21] However, coupling sites composed of metal single atoms (SAs) and clusters (Cs) or nanostructures can achieve synergistic catalysis for the complex hydrogenation of VR.[22–24]

Herein, we designed and constructed a robust Mo SAs–MoS$_2$ coupling catalyst through the reaction induction transformation of Mo SAs–Mo Cs, which we prepared using an encapsulation–pyrolysis–etching strategy. The spontaneous generation of Mo SAs–MoS$_2$ synergistically promoted H$_2$ activation and enhanced local active H concentration, thus enhancing the efficient conversion of VR. It was also found that the enhancement of active H concentration avoids the continuous aggregation and marginal growth deactivation of the MoS$_2$ catalyst during the hydrogenation reaction. Density functional theory (DFT) calculations showed that the synergistic actions of the Mo SAs–MoS$_2$ coupling catalyst reduced the adsorption energy barriers for H$_2$ and anthracene, which significantly promoted the hydrogenation. These findings provide a novel idea for the design of efficient coupling catalysts by controlling local hydrogen species concentration for enhancing hydrogenation reactions.

Results and discussion

Synthesis and spontaneous generation of the Mo SAs–MoS$_2$ coupling catalyst

The Mo SAs–MoS$_2$ coupling catalyst was prepared by the reaction induction transformation of Mo SAs–Mo Cs, which were synthesized by an encapsulation–pyrolysis–etching strategy (Fig. 1). First, coal tar pitch (CTP) was selected as the carbon precursor because of its good oil solubility and high carbon

graphitization. Next, melamine and ammonium molybdate molecules with oxygen-bridged [MoO$_4$] tetrahedral units were uniformly dispersed on CTP by strong π–π conjugation. Lamellar MgO was selected as the template for encapsulation, as it can fully integrate with the carbon substrate in pyrolysis. Then, Mo SAs–Mo Cs with a Mo content of 5.37 wt% were obtained by acid etching the MgO template. The Mo SAs–MoS$_2$ could be generated spontaneously by the *in situ* sulfurization reaction induction transformation of Mo SAs–Mo Cs. It should be emphasized that the S species mainly originated from heavy oil. The synthesized Mo SAs–Mo Cs exhibited a significant Brunauer–Emmett–Teller (BET) surface area of 504 m^2 g^{-1} and pore size of 3 nm, as determined by N$_2$ physical adsorption/desorption (Fig. S1, ESI†). This large surface area and pore size are favorable for the carbon-supported capture of metal species and can improve mass transfer during the hydrogenation of VR. The 3D lamelliform-like structure with abundant pores was confirmed by scanning electron microscopy (SEM) (Fig. S2, ESI†).

The X-ray diffraction (XRD) patterns of the Mo SAs–Mo Cs (Fig. S3, ESI†) showed broad peaks of 26° attributed to the amorphous carbon for the (002) plane, excluding the presence of metal nanoparticles or oxide crystals in the Mo SAs–Mo Cs. The transmission electron microcopy (TEM) images further showed the lamelliform-like carbon morphologies (Fig. S4a, ESI†). No visible metal nanoparticles (Fig. S4b, ESI†) could be discovered in the Mo SAs–Mo Cs by high-resolution TEM (HRTEM). Moreover, high-angle annular dark-field scanning transmission electron microscopy (HAADF-STEM) indicated the presence of metal Mo clusters. The energy-dispersive spectroscopy (EDS) mapping confirmed the uniform distribution of Mo, O, N, and C species in the Mo SAs–Mo Cs (Fig. S4c, ESI†). Aberration-corrected HAADF-STEM (AC-HAADF-STEM) images (Fig. 2a and b) were obtained and further revealed the uniform dispersion of metal Mo clusters and Mo SAs. As shown in Fig. 2c, the sizes of the Mo clusters were about 6–7 Å,
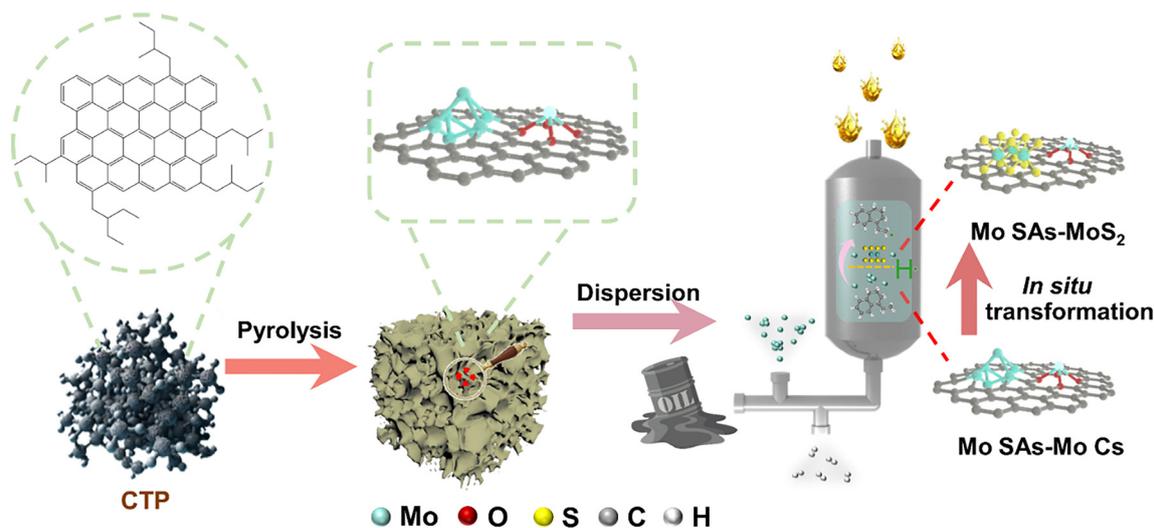

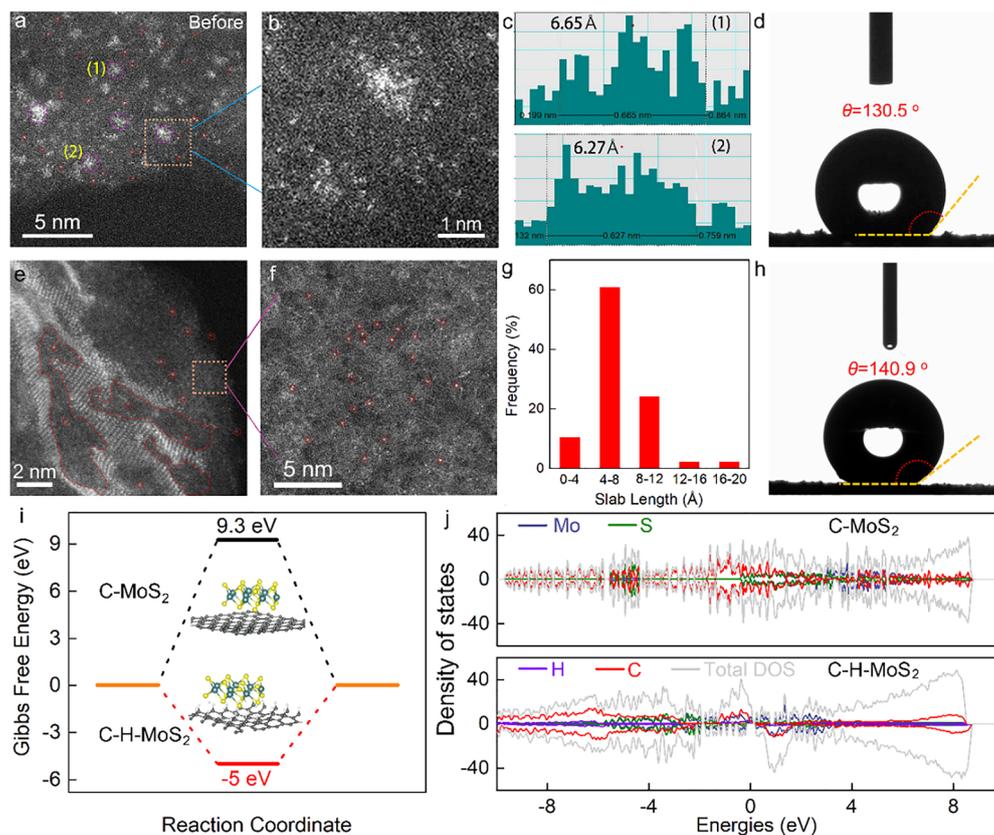**Fig. 1** Schematic of the catalyst preparation process.

Fig. 2   Structural evolution of Mo SAs–Mo Cs into the Mo SAs–MoS$_2$ catalyst. (a) and (b) AC-HAADF-STEM images, (c) cluster size distribution of areas (1) and (2) in (a), (d) corresponding contact angle of Mo SAs–Mo Cs. (e) and (f) AC-HAADF-STEM images, (g) corresponding distribution of the slab lengths of the MoS$_2$ nanosheets, and (h) corresponding contact angle of Mo SAs–MoS$_2$. MoS$_2$ adsorption on C and C–H substrates and (i) the variations of the Gibbs free energy, and (j) pDOS of the Mo 3d, S 2s, H 1s, C 1s orbitals, and total DOS.

respectively. In addition, the Mo SAs–Mo Cs showed good hydrophobicity with static angles of 130.5° (Fig. 2d), which revealed their superior oil solubility.

Two typical peaks at 34° (100) and 59° (110) in the XRD pattern were attributed to MoS$_2$ in the Mo SAs–MoS$_2$ (Fig. S3, ESI†). HRTEM (Fig. S4d, ESI†) demonstrated that the MoS$_2$ crystal phase was generated during the hydrogenation reaction in VR. Also the AC-HAADF-STEM (Fig. 2e, f) images demonstrated that most Mo atoms could be embedded into the MoS$_2$ lattice. Combined with the characterization of the Mo SAs–Mo Cs precursor, it was confirmed that the Mo species were partly transformed from clusters into MoS$_2$, while the Mo SAs retained atomic dispersion characteristics (Fig. S5, ESI†).[12,13] The length statistics showed that the slab lengths of MoS$_2$ were mainly in the range of 4–12 Å. However, a large number of Mo SAs were distributed between the MoS$_2$ layers. This indicated that the Mo SAs induced the oriented growth of MoS$_2$ by activating H$_2$. Sulfurization experiments for Mo species with different gases were further used to prove the above inference. From the TEM images in H$_2$ (Fig. S7a–c, ESI†) and N$_2$ (Fig. S7d–f, ESI†) atmospheres, the MoS$_2$ nanosheets were denser in H$_2$ than in N$_2$, which demonstrated the induced growth of MoS$_2$ sheets under H$_2$. Moreover, the variations of the Gibbs free energies (Fig. 2i and Fig. S6, ESI†) for MoS$_2$ adsorption on the

substrate were further studied on the C and active H-adsorbed C surfaces. It was found that MoS$_2$ adsorption was considerably more favorable on C–H surfaces than on the C surfaces. Compared to the C substrate, the pDOS in the C–H substrate (Fig. 2j) indicated that the covalent bonds were strongly aggregated near the Fermi level.[25] This active hydrogen was beneficial for the adsorption of MoS$_2$ on the substrate and could therefore avoid the continuous growth of MoS$_2$. The Mo SAs–MoS$_2$ catalyst also showed good hydrophobicity with a static angle of 140.9° (Fig. 2h), about 10° more than the Mo SAs–Mo Cs precursor, which further indicated that the Mo SAs–MoS$_2$ catalyst could be well dispersed in VR, revealing its better hydrogenation performance.

Structural evolution of Mo SAs–Mo Cs into the Mo SAs–MoS$_2$ catalyst

To further explore the local structural evolution upon the spontaneous generation of active sites, XPS was performed and the spectra of the Mo SAs–Mo Cs and Mo SAs–MoS$_2$ catalysts were compared (Fig. 3a). Because of the *in situ* change in the type of Mo species, the Mo 3d spectra were analyzed. The valence state of Mo species in Mo SAs–Mo Cs was mainly Mo^{6+}, while in Mo SAs–MoS$_2$, Mo species with +4 and +5 valence states were generated at a much higher content than Mo^{6+},
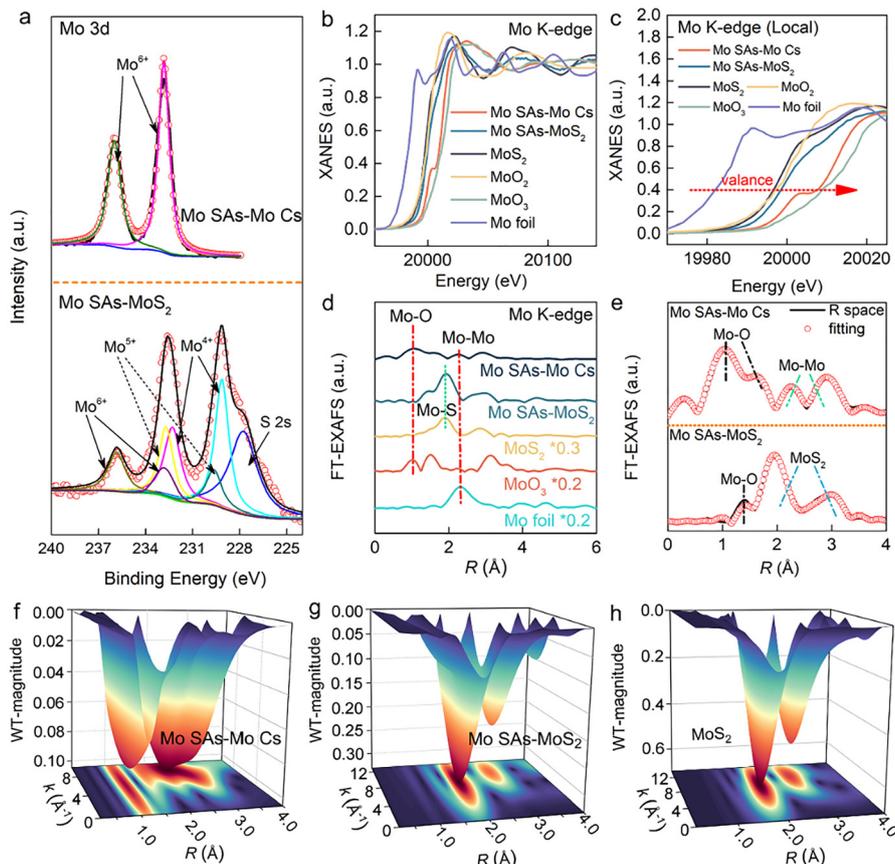
Fig. 3 Local structural evolution of Mo SAs–Mo Cs into Mo SAs–MoS$_2$ catalysts. (a) XPS spectra, Mo K-edge in (b) XANES and (c) adsorption edge, (d) EXAFS and (e) EXAFS fitting curves. WT contour plots of (f) Mo SAs–Mo Cs, (g) Mo SAs–MoS$_2$, and (h) MoS$_2$.

indicating that Mo was mainly in the +6 state, and the valences of the Mo species in MoS$_2$ were mainly +4 and +5. The work function of Mo SAs–Mo Cs (4.72 eV) and Mo SAs–MoS$_2$ (4.48 eV) were analyzed by UPS (Fig. S8, ESI†), which further inferred that the valence state of the Mo species decreased during the reaction.

The fine structure of the catalysts was further analyzed by X-ray absorption spectroscopy (XAS). Also, X-ray absorption near-edge spectroscopy (XANES) was performed as it can reflect information on the valence state and local configuration (Fig. 3b). The observed shift of $\Delta\mu_0$ (edge step) demonstrated there was a change in the valence state (Fig. 3c), wherein the Mo K-edges of Mo SAs–Mo Cs and Mo SAs–MoS$_2$ were located between the MoO$_2$ and MoO$_3$ standard, suggesting the average valence states of the Mo species were close to +4 and +6, respectively. The valence state is related to the coordination environment of metal species. The EXAFS curves (Fig. 3d and Fig. S9, ESI†) showed peaks in the R space of 1.04 and 1.4 Å, ascribed to Mo–O coordination. The peaks at 1.93 and 2.85 Å could be assigned to the Mo–S coordination and the peak at 2.31 Å was ascribed to Mo–Mo coordination. Two effective peaks appeared at 1.1 and 2.4 Å^{-1} in the WT-EXAFS of Mo SAs–Mo Cs (Fig. 3f), corresponding to Mo–O and Mo–Mo, respectively (Fig. S10, ESI†). In addition, peaks for Mo–O and Mo–S of Mo SAs–MoS$_2$ were observed at 2.0 and 2.9 Å^{-1}

(Fig. 3g and h), in contrast to the MoS$_2$ standard, further demonstrating the local structural evolution of Mo SAs–Mo Cs into Mo SAs–MoS$_2$. Moreover, the EXAFS fitting curves (Fig. 3e) showed that the Mo–O and Mo–Mo coordination numbers were about 4 and 6 in Mo SAs–Mo Cs, while the Mo–O and Mo–S coordination numbers were about 4 and 2 after the EXAFS fitting for Mo SAs–MoS$_2$, respectively (Table S2, ESI†). For comparison, the Mo SAs catalyst exhibited a Mo–O isolate configuration through XAS analysis (Fig. S11a and b, ESI†), wherein the EXAFS fitting results demonstrated a greater degree with a Mo–O coordination number of 3.62 (Fig. S11c, d and Table S2, ESI†).

Hydrogenation performance of VR

The catalytic hydrogenation evaluation of VR was conducted in an autoclave with H$_2$ at 7 MPa and 425 °C for 1 h. The pressure drop curve illustrates the H$_2$ consumption in the reaction system within 1 h (Fig. S12, ESI†). The Mo SAs–MoS$_2$ catalyst produced the maximum pressure drop, indicating the maximum hydrogen consumption among all the catalysts. Fig. 4a illustrates the distribution of the product fractions obtained using different catalysts for the hydrogenation of VR. In the absence of a catalyst, coke formation (9.5 wt%) and gas formation (9.4 wt%) were detected. The Mo SAs–MoS$_2$ catalyst showed the best coke inhibition performance, with the lowest
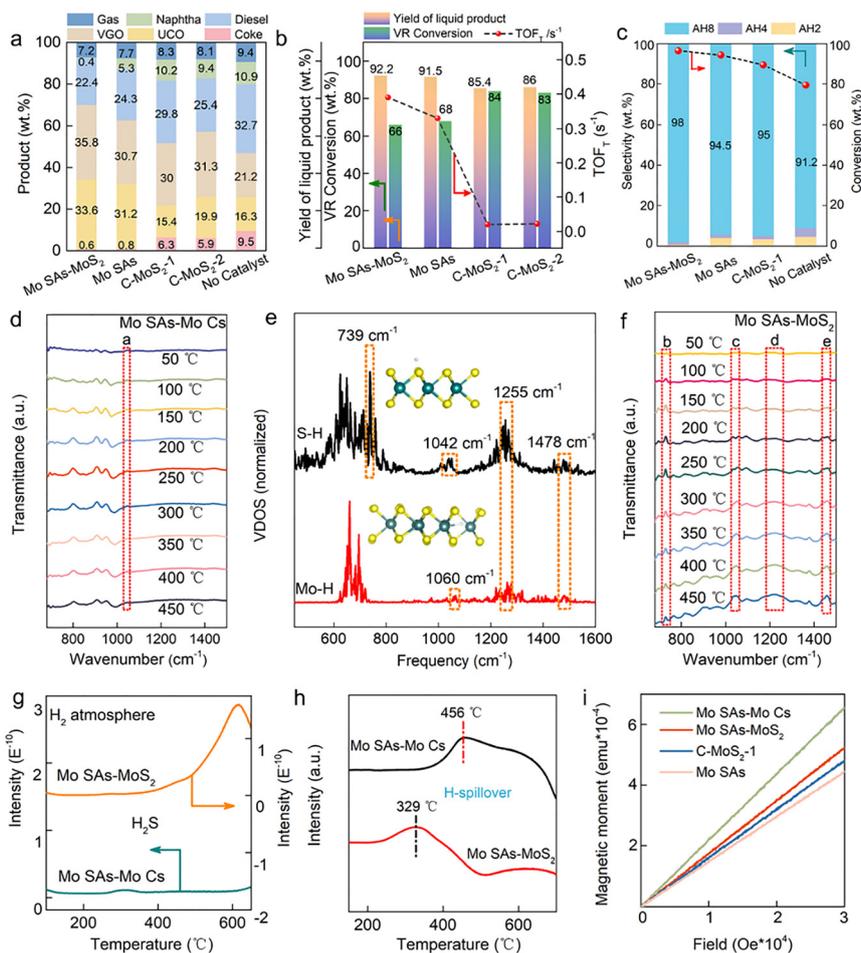
Fig. 4 Hydrogenation performance and mechanism of Mo SAs−MoS₂ in the VR slurry phase at 698 K. (a) Yield of different products. (b) Liquid product yields, VR conversion, and TOF_T. (c) Anthracene hydrogenation performance tests in the slurry phase, including anthracene conversion and product selectivity. *In situ* DRIFTS spectra in H₂ for (d) Mo SAs−Mo Cs. (e) Theoretical peaks of the dissociative adsorption of H on the Mo site and S site at 698 K obtained through AIMD simulation. (f) Mo SAs−MoS₂. Comparison of the Mo SAs−Mo Cs precursor and Mo SAs−MoS₂ catalysts. (g) Mass spectrum. (h) H₂-TPR. (i) PPMS.

coke yield of 0.6 wt%, which was lower than that of the Mo SAs (0.8 wt%), and carbon-supported MoS₂ catalysts (C-MoS₂-1 with a coke yield of 6.3 wt% and C-MoS₂-2 with 5.9 wt%), respectively. The liquid product yield and VR conversion (Fig. 4b) could be obtained by analyzing the obtained products in Fig. 4a. Mo SAs−MoS₂ exhibited an excellent liquid product yield and per pass conversion of VR of 92 wt% and 66 wt%, respectively. Mo SAs (Fig. S13 and S14, ESI†) also showed good product yields, but slightly inferior to Mo SAs−MoS₂. C-MoS₂-1 and C-MoS₂-2 with poor activity showed lower liquid product yields.

To further verify the hydrogenation capacity of the prepared catalysts, the total turnover frequency (TOF_T) was calculated and it exhibited a tight relationship with H₂ consumption and the total metal addition. Specifically, Mo SAs−MoS₂ achieved the highest TOF_T of 0.39 s⁻¹, which was higher than that of Mo SAs, C-MoS₂-1 and C-MoS₂-2 of 0.33, 0.02 and 0.022 s⁻¹, respectively. All these hydrogenation performance tests and analyses indicated that the prepared Mo SAs−MoS₂ catalyst have a superior H₂-activation capability (Table S3, ESI†). Compared with Mo SAs and C-MoS₂ catalysts, Mo SAs−MoS₂ showed

better hydrogenation activity. Therefore, anthracene was select as a model compound[26] for the hydrogenation experiments to further investigate the synergistic effect between Mo SAs and MoS₂. As depicted in Fig. 4c, the anthracene conversions of Mo SAs−MoS₂, Mo SAs, and C-MoS₂-1 catalysts were 96.6, 94.5, and 89.6 wt%, respectively, all higher than the 79.6 wt% achieved without a catalyst. Product analysis exhibited that the Mo SAs−MoS₂ catalyst had higher selectivity for 8-hydroanthracene (AH8) than Mo SAs and C-MoS₂-1, indicating that the synergy between Mo single atoms and MoS₂ promoted a deep hydrogenation of the aromatic hydrocarbons, which could also explain the higher TOFs and different product compositions of Mo SAs−MoS₂. Furthermore, the anthracene hydrogenation with cyclic regeneration of the catalyst was conducted at 425 °C and a 7 MPa H₂ initial pressure (Fig. S15, ESI†). The conversion was reduced from 96.6 wt% to about 92 wt%, while the selectivity for 8-hydroanthracene (AH8) was basically unchanged, which was mainly due to the loss of catalyst during the cycle test. Thus, the Mo SAs−MoS₂ catalyst demonstrated good cycling stability.

Hydrogenation mechanism

To further investigate the synergistic effect between MoS_2 and Mo SAs, *in situ* characterization was performed to verify the dynamic changes in the active hydrogen species in the reaction. *In situ* H_2 diffuse reflectance infrared Fourier transform spectroscopy (DRIFTS) was carried out for different temperatures from 50 °C to 450 °C (Fig. 4d and f). S–H and Mo–H stretching vibration peaks were obtained by AIMD simulation at 698 K as theoretical values. The peaks around 739, 1042, 1255, 1478 cm^{-1} were ascribed to the S–H bonds, and the peaks around 1060, 1255, 1478 cm^{-1} corresponded to Mo–H bonds.[27] The peak b in Mo SAs–MoS_2 was ascribed to S–H species, while peak a attributed to Mo–H species. In addition, peaks c, d, e were ascribed to Mo–H or S–H species. Thermogravimetry (TG) analysis was next performed to analyze the dispersion of H species in the catalysts. The weight loss curves were observed at 357–461 °C and 235–432 °C, respectively (Fig. S16, ESI†), which indicated different products for Mo SAs–Mo Cs and Mo SAs–MoS_2. From the mass spectra (Fig. 4g), more H_2S was detected in Mo SAs–MoS_2 ($\sim 2 \times 10^{-10}$) than Mo SAs–Mo (close to zero). However, the formation of NH_3 was similar in the two catalysts as 2×10^{-9} and 1.6×10^{-9} (Fig. S17, ESI†). Compared with the yields of H_2S and NH_3, the hydrogen species were more concentrated near the S species. As shown in Fig. 4h, H spillover was verified from the H_2-TPR spectra, and the reduction temperature decreased from 456 °C for Mo SAs–Mo Cs to 329 °C for Mo SAs–MoS_2, which indicated that the H_2 was activated to form active H, which adsorbed on to the surface of Mo SAs–MoS_2 during hydrogenation. As a result, the reduction temperature of Mo SAs–MoS_2 was significantly decreased more than that of Mo SAs–Mo Cs, indicating the existence of hydrogen spillover during the hydrogenation.[28–31] The weak adsorption of H_2 by the Mo SAs-Cs precursor indicated that the Mo clusters lacked the ability to improve hydrogen spillover, which made it difficult for hydrogen to migrate and desorb at high temperature. The strong chemisorption (450 °C) of the Mo single-atom site in the Mo SAs–MoS_2 catalyst accelerated the adsorption and dissociation of H_2, while the *in situ* generation of MoS_2 significantly changed the adsorption behavior of H_2. Furthermore, the surface acceptor site received the H atoms migrated by the Mo single atom to form a weak adsorption species, resulting in the appearance of the low-temperature desorption peak (227 °C).

In addition, the number of vacancies in Mo SAs–MoS_2 was higher than that in Mo SAs–Mo Cs (Fig. S19, ESI†). The induction of active hydrogen was a necessary condition for the formation of oxygen vacancies, which further verified that the H_2 was activated and spilled over to the surface of the catalyst.[32,33] Magnetic measurements are often used to determine the unsaturated electrons in a sample. Here, physical property measurement system (PPMS) tests were performed and the results demonstrated that the unsaturated electron contents of the prepared precursor and catalysts followed the order: Mo SAs–Mo Cs > Mo SAs–MoS_2 > C-MoS_2-1 > Mo SAs (Fig. 4i). Compared with Mo SAs–Mo Cs and Mo SAs, it could be inferred that the unsaturated electrons of the Mo SAs–Mo Cs were more

derived from the Mo clusters. Moreover, compared with the Mo SAs–MoS_2 and C-MoS_2-1 catalysts, the single Mo atoms in Mo SAs–MoS_2 were the main origin of the unsaturated electrons, which indicated that the active hydrogen adsorbed on the surface of Mo atoms after activation migrated to the vacancies in MoS_2, further inhibiting the continuous growth of MoS_2. Electrochemical impedance spectroscopy (EIS) was next carried out to explore the conductivity of the catalysts (Fig. 5a). The charge-transfer resistance of the precursor and catalysts were in the order of Mo SAs–Mo Cs < Mo SAs–MoS_2 < C-MoS_2-1 < Mo SAs. A high resistivity corresponds to less unsaturated electrons in the catalyst, which further supports the inference obtained by PPMS.

Theoretical evidence of hydrogenation for Mo SAs–MoS_2

DFT calculations were performed to investigate the synergistic effect of Mo SAs and MoS_2 for H_2 activation and anthracene adsorption. Several types of Mo species supported on the plane of a C matrix, including C-Mo, C-MoS_2, C-Mo–MoS_2, were selected as reference prototypes to understand the hydrogenation in the slurry phase (Fig. S20–S22, ESI†). The catalytic behaviors of Mo species showed a remarkable correlation with their exposed active sites. As shown in Fig. 5b, the free energy of H_2 adsorption (ΔG_H) for C-Mo–MoS_2 was −5.3 eV, which was significantly higher (in absolute terms) compared to that of C-Mo and C-MoS_2, as −1.5 eV and −1.6 eV, respectively. The much lower ΔG_H indicated that the synergistic effect of Mo SAs and MoS_2 promoted the adsorption and dissociation of H_2. The charge-density-difference plots (Fig. 5c) suggested that substantial charge transfer occurred from the single Mo and the edge of MoS_2 sites to the adsorbed H sites. Significant charge depletion was observed on Mo and S sites, indicating a mixed characteristic of covalent and ionic bonds for the Mo–H and S–H interactions. Hydrogen spillover constrained the marginal growth of MoS_2, and the corresponding transition state in each elementary step was demonstrated in Fig. 5d. The control step of hydrogen spillover exhibited ideally low H-transport barriers of 1.22 eV, which demonstrated a favorable potential for H migration. The MoS_2 in the C basal plane could barely adsorb anthracene. However, anthracene could adsorb on the single Mo site in the C basal plane with a low barrier of −3.2 eV. In comparison, the adsorption of anthracene at the single Mo and MoS_2 co-sites was favorable with clearly lower barriers of −3.5 eV (Fig. 5e). The charge-density-difference plots (Fig. S23, ESI†) suggested that the adsorption process of anthracene on the catalyst surface had a large amount of charge transfer with single atom Mo, while MoS_2 mainly had a steric effect, which increased the adsorption instability of anthracene. Fig. 5f illustrates the calculated density of states (DOS) for the Mo d orbitals. One can see that for the C-Mo–MoS_2 model, the distribution of d states in energy space (indicated by the gray line) was narrow and predominantly situated away from the Fermi level. Conversely, for the C-Mo–MoS_2-H_2 and C-Mo–MoS_2-en systems, the d states (represented by the orange and blue line) were more widespread and made a large contribution near the Fermi level. This implied that the C-Mo–MoS_2 can
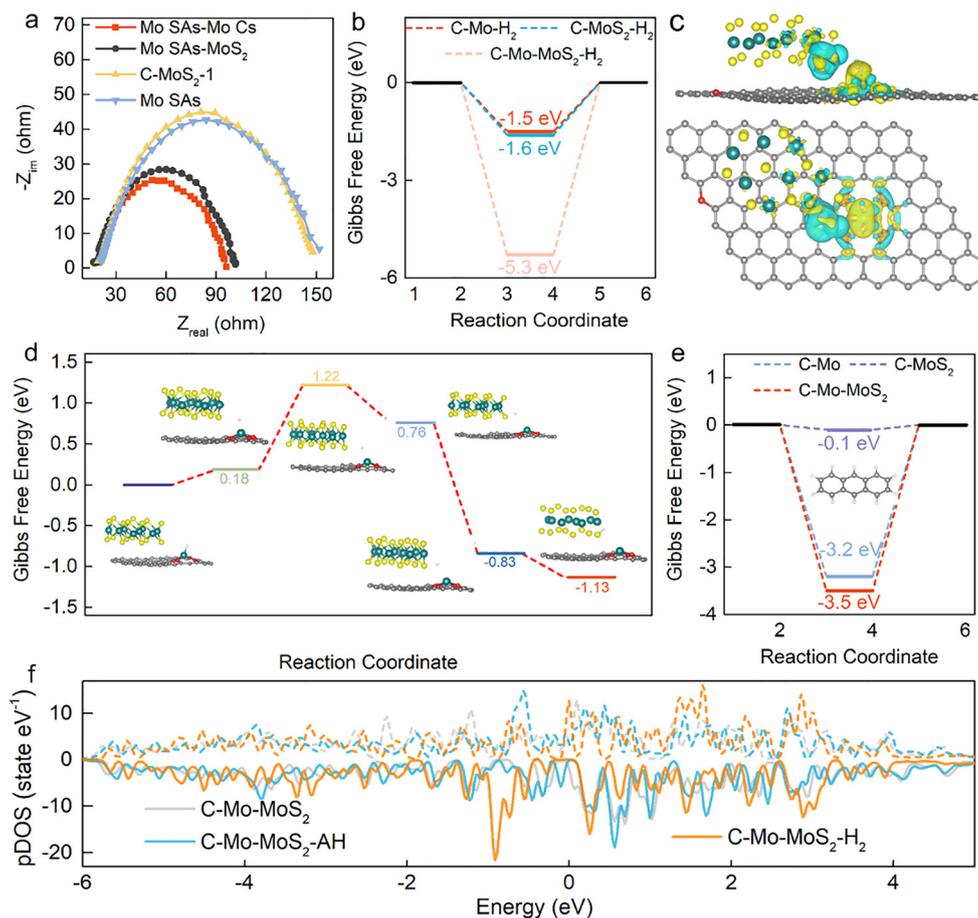
Fig. 5 Catalytic mechanism investigation. (a) EIS spectra of Mo SAs–Mo Cs, Mo SAs–MoS$_2$, C-MoS$_2$-1, and Mo Sas. (b) H$_2$ adsorption energy and (c) charge density under basic conditions in C-Mo, C-MoS$_2$, and C-Mo–MoS$_2$. Yellow and cyan regions represent electron accumulation and depletion. (d) Energy barrier of the hydrogen spillover transition state from the Mo single atom to MoS$_2$. (e) Anthracene adsorption energy under basic conditions in C-Mo, C-MoS$_2$, C-Mo–MoS$_2$. (f) pDOS of C-Mo–MoS$_2$, C-Mo–MoS$_2$-AH, and C-Mo–MoS$_2$-H$_2$.

bond and engage more effectively with H$_2$ and anthracene and therefore will play a more active role in the hydrogenation of VR.

Conclusions

In summary, we report a robust Mo SAs–MoS$_2$ coupling catalyst for the slurry-phase hydrogenation of VR. The Mo SAs–MoS$_2$ catalyst was constructed by a reaction induction transformation strategy. The spontaneous generation of the Mo SAs–MoS$_2$ coupling catalyst synergistically promotes H$_2$ activation and enhances the local active hydrogen concentration in the hydrogenation of VR. The yield of liquid product was 92 wt%, and the coke only content was 0.6 wt% with a TOF$_T$ of 0.39 s^{-1}. It was also found that the enhancement of the active H concentration avoided the continuous aggregation and growth and deactivation of the MoS$_2$ catalyst during the hydrogenation reaction. Theoretical calculations revealed that the synergistic effects of the Mo SAs–MoS$_2$ coupling catalyst facilitated electron transfer between the Mo species and reactants, reducing the adsorption energy barriers for H$_2$ and anthracene. The control step for hydrogen spillover exhibited an ideally low H-transport barrier of 1.22 eV, which demonstrates a favorable potential for H migration. This work provides a novel idea for the design of an efficient coupling catalyst for strengthening local active hydrogen concentration in the hydrogenation of VR, and this concept also can be applied to other hydrogenation systems. This study provides a new perspective for designing beneficial coupling hydrogenation catalysts with strengthening the local active hydrogen concentration, which would be beneficial for a series of hydrogenation systems.

Experimental

Chemicals and materials

Vacuum residue (VR) was obtained from Qingdao Refining (Table S1, ESI†). Coal tar pitch (CTP) was obtained from Hebei Hankai Energy Technology Development Co., Ltd. Ammonium molybdate tetrahydrate (AR), melamine (C$_3$H$_6$N$_6$, 99%), magnesium oxide (AR, 98%), ethanol (AR), sulfuric acid (70%), anthracene (GC, 99%), tridecane (GC, 99%), and molybdenum disulfide (99%) were purchased from Aladdin.

Catalyst preparation

Preparation of lamellar magnesium oxide. First, 500 mL deionized water was put into a flask, and 50 g MgO was added.

The mixture was stirred evenly, heated and re-fluxed for 8 h (the temperature of the oil bath was set at 100 °C), and then filtered after naturally cooling. The obtained filter cake was wrapped with filter paper and placed in an oven at 110 °C for 12 h. The dried filter cake was ground into powder and calcined in a muffle furnace at 550 °C for 1 h to obtain lamellar MgO.

Preparation of Mo SAs–Mo Cs. First, 1 g CTP and 1 g melamine were dispersed in 40 mL ethanol, and ultrasonicated for 30 min to disperse evenly, and this was marked as solution A. Meanwhile, 600 mg ammonium molybdate tetrahydrate was dissolved in 40 mL deionized water and sonicated for 30 min to completely dissolve, and this was marked as solution B. Then, solutions A and B were mixed under stirring, and 1 g lamellar magnesium oxide was added to the above mixed solution. After stirring for 24 h and drying in the oven at 70 °C, the catalyst precursor was obtained. The catalyst precursor was placed in a crucible and calcined at 650 °C for 4 h in a N_2 atmosphere. Thus, the Mo SAs–Mo Cs precursor was obtained after acid etching the black powder. Here, 0.5 mol L^{-1} sulfuric acid solution was used for the acid etching process, and this step was maintained for 12 h.

Spontaneous generation of the Mo SAs–MoS$_2$ catalyst. With the initial H_2 pressure of 7 MPa in the reaction, and rise to 425 °C at the rate of 8 °C min^{-1}. The sulfur-rich environment (sulfur compounds) in the hydrogenation of heavy oil promotes the direct conversion of Mo SAs–Mo Cs into the Mo SAs–MoS$_2$ catalyst.

Preparation of Mo SAs. First, 1 g CTP and 1 g melamine were dispersed in 40 mL ethanol, and ultrasonicated for 30 min to disperse evenly, and this was marked as solution C. Meanwhile, 30 mg ammonium molybdate tetrahydrate was dissolved in 40 mL deionized water and sonicated for 30 min to completely dissolve, and this was marked as solution D. Then, solutions C and D were mixed under stirring, and 1 g lamellar magnesium oxide was added to the above mixed solution. After stirring for 24 h and drying in the oven at 70 °C, the catalyst precursor was obtained. The catalyst precursor was then placed in a crucible and calcined at 650 °C for 4 h in N_2 atmosphere. Thus, the Mo SAs catalyst was obtained after acid etching the black powder.

Preparation of C-MoS$_2$-1. First, 1 g CTP and 1 g melamine were dispersed in 40 mL ethanol, and ultrasonicated for 30 min to disperse evenly, and this was marked as solution E. Next, 1 g lamellar magnesium oxide was added to solution E. After stirring for 24 h and drying in the oven at 70 °C, the solid F was obtained. Solid F was then placed in a crucible and calcined at 650 °C for 4 h in a N_2 atmosphere to obtain solid G. Then, solid G was mixed with 200 mg MoS$_2$ in 100 mL ethyl alcohol, dispersed, and dried, to obtain solid H. Finally, solid H was placed in a crucible and calcined at 650 °C for 4 h in a N_2 atmosphere and the C-MoS$_2$-1 catalyst was obtained after acid etching the black powder.

Preparation of C-MoS$_2$-2. First, 1 g CTP and 1 g melamine were dispersed in 40 mL ethanol, and ultrasonicated for 30 min to disperse evenly, and this was marked as solution I. Meanwhile, 200 mg MoS$_2$ was dissolved in 40 mL deionized water and sonicated for 30 min to completely dissolve, and this was marked as solution J. Then, solution I and J were mixed under

stirring, and 1 g lamellar magnesium oxide was added to the above mixed solution. After stirring for 24 h and drying in the oven at 70 °C, the catalyst precursor was obtained. The catalyst precursor was placed in a crucible and calcined at 650 °C for 4 h in a N_2 atmosphere. Thus, the Mo SAs catalyst was obtained after acid etching the black powder.

Catalyst characterization

N_2 physical adsorption/desorption analysis was performed using a Micrometritics ASAP2020 instrument. Inductively coupled plasma-optical emission spectrometry (ICP-OES) measurements were carried out using a Thermo Scientific Icap 6300 system. X-Ray diffraction (XRD) analysis was conducted using a Panalytical X'pert PRO X-ray diffractometer equipped with a Cu Kα radiation source. Scanning electron microscopy (SEM) was performed using a Hitachi S-4800 electron microscope. High-resolution transmission electron microscopy (HRTEM) and high-angle annular dark-field scanning transmission electron microscopy (HAADF-STEM) with energy-dispersive X-ray spectroscopy (EDS) mapping were performed using a JEOL-2100F electron microscope operating at a working voltage of 200 kV. Aberration-corrected HAADF-STEM was performed on a Titan 80-300 microscope operating at a working voltage of 300 kV. Synchrotron X-ray absorption spectroscopy (XAS) was carried out at the stations of the Shanghai Synchrotron Radiation Facility (SSRF), specifically at Beamlines 11B (BL11B) and 13SSW (BL13SSW). XAS measurements were performed at the Mo K-edge in the fluorescence mode using a Lytle detector. *In situ* diffuse reflectance infrared Fourier transform spectroscopy (DRIFTS) tests were captured using a Bruker VERTEX 70V FTIR spectrometer. X-Ray photoelectron spectroscopy (XPS) was performed using an ESCALAB MK II spectrometer equipped with an Al Kα (1486.6 eV) monochromated photon source and two ultrahigh vacuum (UHV) chambers. Electron spin resonance (ESR) spectroscopy was carried out using a Bruker EMX Plus spectrometer. Physical property measurement system (PPMS) tests were performed using an America-Quantum Design-PPMS 16T instrument.

Catalyst evaluation

The catalytic performance of the catalysts in hydrocracking was evaluated using a batch mode experiment in a 500 mL autoclave. VR (100 g) was used as the feedstock. The experiments were carried out at a reaction temperature of 425 °C and an initial hydrogen pressure of 7 MPa, utilizing Mo SAs–MoS$_2$ catalyst at a concentration of 200 ppm, calculated based on the weight of molybdenum. The reaction was maintained under a stirring speed of 500 rpm for a duration of 1 h. After the reaction, the autoclave was brought down to room temperature, following which the gas products were expelled. The toluene-insoluble components within the product were identified as coke deposits and the catalyst. The fractionation distribution of the liquid product was analyzed *via* the gas chromatography-simulated distillation (GC-SD) methodology. This GC-SD methodology segregates the liquid product into four distinct fractions: unconverted oil (UCO, boiling point > 500 °C), vacuum

gas oil (VGO, boiling range 350–500 °C), diesel fraction (boiling range 180–350 °C), and naphtha fraction (boiling point <180 °C). The mass of the vapor phase output was ascertained by deducting the weight of the liquid product and the toluene-insoluble components from the total reactor volume. The anthracene hydrogenation activity of the Mo SAs–MoS$_2$ catalysts was evaluated in a batch-wise manner using a 200 mL autoclave setup. In the reaction, Mo SAs–MoS$_2$ (0.5 g), anthracene (4 g) and tridecane (50 g) served as the reactants, with the catalyst being simultaneously incorporated into the reaction mixture. The experiments aimed at anthracene hydrogenation were performed under a reaction temperature of 425 °C and an initial hydrogen pressure of 7 MPa. The reaction conditions were maintained with a stirring speed of 700 rpm for 4 h. After the reaction, the product was cooled to room temperature using the autoclave. The products were analyzed using liquid chromatography and included octahydroanthracene (AH8), tetrahydroanthracene (AH4), and dihydroanthracene (AH2).

The calculations of the liquid product yield and VR conversion were performed using the following equations:

$$\text{Yield of liquid products (wt\%)} = \text{Yields of (naphtha + diesel +} \\ \text{VGO + UGO)}$$

$$\text{VR conversion (wt\%)} = \frac{\text{UCO in (VR} - \text{product)}}{\text{UCO in VR}}$$

TOF$_T$ was calculated using the following equation:

$$\text{TOF}_T \ (\text{s}^{-1}) = \frac{\text{Hydrogen consumption rate (mol s}^{-1})}{\text{Number of total metal atoms (mol)}}$$

The conversion and selectivity for the hydrogenation products of anthracene were calculated using the following equations:

$$\text{Anthracene conversion (wt\%)} = \frac{\text{Anthracene in products}}{\text{Anthracene in reactant}}$$

$$\text{Products selectivity (wt\%)} = \frac{\text{Different product content}}{\text{Total amount of products}}$$

Computational details

All the computations using density functional theory (DFT) were conducted with the Vienna Ab initio Simulation Package (VASP) version 5.4.4.[34,35] The Perdew–Burke–Ernzerhof (PBE) functional, based on the generalized gradient approximation (GGA), was employed to describe the exchange–correlation energy.[36] The projector-augmented wave (PAW) pseudopotential was utilized to account for the interaction between ions and electrons. The Grimme approach (DFT-D3) was applied to correct for weak van der Waals interactions. The kinetic energy cut-off for the plane-wave expansion was set to 450 eV. A $3 \times 3 \times 1$ Monkhorst–Pack k-point grid was used for efficient structure optimizations. The convergence criteria for the energy and forces were set to 1×10^{-5} eV and 0.03 eV Å^{-1}, respectively. The identification of the transition states was achieved using

the climbing image nudged elastic band method (CI-NEB). A meticulously constructed model of single-layer graphene, exhibiting periodic repetition, was established with a unit cell dimension of 6×6 and a vacuum slab height of 25 Å.

The adsorption energies of hydrogen were calculated using the formula $\Delta G = G_{\text{slab+2H}} - G_{\text{slab}} - G_{\text{H}_2\text{(g)}}$, where $G_{\text{slab+2H}}$, G_{slab}, and $G_{\text{H}_2\text{(g)}}$ represent the Gibbs free energy of the catalyst model slab with adsorbed hydrogen, the slab, and gaseous hydrogen, respectively. The Gibbs free energy was calculated according to the equation: $G = E + \text{ZPE} - TS$ where E, ZPE, and S are the DFT-calculated energies, zero-point energies, and entropy, respectively.

Author contributions

Conceptualization: G. S., Y. P. Methodology: G. S., P. X., Y. L., H. S. Investigation: X. Z., F. T., Z. G. Visualization: C. Y., J. L., B. L. Supervision: Y. L. Z. L. Writing – original draft: G. S., Z. L. Writing review & editing: Y. P.

Conflicts of interest

All the authors declare they have no competing interests.

Data availability

The data supporting this article have been included as part of the ESI.†

Acknowledgements

Notes and references

1 E. T. C. Vogt and B. M. Weckhuysen, *Chem. Soc. Rev.*, 2015, **44**, 7342–7370.

2 R. Prajapati, K. Kohli and S. K. Maity, *Fuel*, 2021, **288**, 119686.

3 Y. Ma, W. Wu, J. Zhang, H. Zhang, Z. Cai, Y. Cao, K. Huang and L. Jiang, *Ind. Eng. Chem. Res.*, 2023, **62**, 15459–15468.

4 R. Qu, K. Junge and M. Beller, *Chem. Rev.*, 2023, **123**, 1103–1165.

5 C. Wu, X. Chen, L. Tang, Q. Wei, J. Liang and L. Wang, *ACS Appl. Mater. Interfaces*, 2021, **13**, 10855–10869.

6 K. H. Kang, N. T. Nguyen, D. V. Pham, P. W. Seo, N. Kang, C. W. Lee, M.-C. Chung, C.-H. Kwak, I. Ro, Y.-P. Jeon and S. Park, *J. Catal.*, 2021, **402**, 194–207.

7 K. D. Kim and Y. K. Lee, *J. Catal.*, 2019, **369**, 111–121.

8 S. H. Kim, K. D. Kim and Y. K. Lee, *J. Catal.*, 2017, **347**, 127–137.

9 S. H. Kim, K. D. Kim, D. Lee and Y. K. Lee, *J. Catal.*, 2018, **364**, 131–140.

10 Z. Guan, M. Wang, G. Sun, X. Xue, Y. Chen, Y. Zhang, T. Zhao, H. Shi, C. Feng, Y. Pan and Y. Liu, *Fuel*, 2024, **357**, 129887.

11 A. V. Bekker and I. Livk, *Ind. Eng. Chem. Res.*, 2011, **50**, 3464–3474.

12 G. Sun, D. Liu, M. Li, S. Tao, Z. Guan, Y. Chen, S. Liu, Q. Du, H. Guo, X. Yuan, X. Zhang, H. Zhu, B. Liu and Y. Pan, *Sci. Bull.*, 2023, **68**, 503–515.

13 G. Sun, D. Liu, H. Shi, J. Li, L. Yang, F. Tian, Y. Cui, C. Wang, F. Li, T. Zhao, H. Zhu, B. Liu, Y. Chai, Y. Liu and Y. Pan, *ACS Catal.*, 2024, **14**, 3208–3217.

14 L. Zhang, M. Zhou, A. Wang and T. Zhang, *Chem. Rev.*, 2020, **120**, 683–733.

15 Y. Zhang, Y. Cheng, X. Wang, Q. Sun, X. He and H. Ji, *ACS Catal.*, 2022, **12**, 15091–15096.

16 H. Jin, S. Sultan, M. Ha, J. N. Tiwari, M. G. Kim and K. S. Kim, *Adv. Funct. Mater.*, 2020, **30**, 2000531.

17 Q. Feng, S. Zhao, Q. Xu, W. Chen, S. Tian, Y. Wang, W. Yan, J. Luo, D. Wang and Y. Li, *Adv. Mater.*, 2019, **31**, 1901024.

18 R. Huang, M. Xia, Y. Zhang, C. Guan, Y. Wei, Z. Jiang, M. Li, B. Zhao, X. Hou, Y. Wei, Q. Chen, J. Hu, X. Cui, L. Yu and D. Deng, *Nat. Catal.*, 2023, **6**, 1005–1015.

19 M. Li, G. Sun, Z. Wang, X. Zhang, J. Peng, F. Jiang, J. Li, S. Tao, Y. Liu and Y. Pan, *Adv. Mater.*, 2024, **36**, 2313661.

20 R. Chen, S. Chen, L. Wang and D. Wang, *Adv. Mater.*, 2024, **36**, 2304713.

21 C. Yue, C. Feng, G. Sun, N. Liu, H. Hao, W. Bao, X. Zhang, F. Sun, C. Zhang, J. Bi, Y. Zhou, H. C. Chen, Y. Pan, D. Sun and Y. Lu, *Energy Environ. Sci.*, 2024, **17**, 5227–5240.

22 Y. Wang, M. Qi, M. Conte, Z. Tang and Y. Xu, *Angew. Chem., Int. Ed.*, 2024, e202407791.

23 X. Xu, X. Li, W. Lu, X. Sun, H. Huang, X. Cui, L. Li, X. Zou, W. Zheng and X. Zhao, *Angew. Chem., Int. Ed.*, 2024, **63**, e202400765.

24 W. Ni, J. L. Meibom, N. U. Hassan, M. Chang, Y. C. Chu, A. Krammer, S. Sun, Y. Zheng, L. Bai, W. Ma, S. Lee, S. Jin, J. S. Luterbacher, A. Schüler, H. Chen, W. E. Mustain and X. Hu, *Nat. Catal.*, 2023, **6**, 773–783.

25 Z. Li and C. Yu, *Nano. Mater.*, 2024, 185–224.

26 P. Zhang, M. Guo, F. Wang, Q. Tang, H. Ge, S. Guo, L. Zhou, X. Li, J. Dong, M. Tang and L. Liu, *J. Mater. Sci.*, 2024, **59**, 21027–21039.

27 R. M. Ramadan, M. S. A. Hamaza and S. A. Ali, *J. Cood. Chem.*, 1998, **43**, 31–39.

28 H. Kang, L. Zhu, S. Li, S. Yu, Y. Niu, B. Zhang, W. Chu, X. Liu, S. Perathoner, G. Centi and Y. Liu, *Nat. Catal.*, 2023, **6**, 1062–1072.

29 M. Xiong, Z. Gao and Y. Qin, *ACS Catal.*, 2021, **11**, 3159–3172.

30 K. Liu, P. Yan, H. Jiang, Z. Xia, Z. Xu, S. Bai and Z. C. Zhang, *J. Catal.*, 2019, **369**, 396–404.

31 Q. Yu, T. Yu, H. Chen, G. Fang, X. Pan and X. Bao, *J. Energy Chem.*, 2020, **41**, 93–99.

32 Y. Yang, S. Zhao, F. Bi, J. Chen, Y. Li, L. Cui, J. Xu and X. Zhang, *Cell Rep. Phys. Sci.*, 2022, **3**, 101011.

33 L. Liccardo, M. Bordin, P. M. Sheverdyaeva, M. Belli, P. Moras, A. Vomiero and E. Moretti, *Adv. Funct. Mater.*, 2023, **33**, 2212486.

34 G. Kresse and J. Furthmüller, *Comput. Mater. Sci.*, 1996, **6**, 15–50.

35 G. Kresse and J. Furthmüller, *Phys. Rev. B: Condens. Matter.*, 1996, **54**, 11169.

36 J. P. Perdew, K. Burke and Y. Wang, *Phys. Rev. B: Condens. Matter Mater. Phys.*, 1998, **54**, 16–533.